Int J Multiphase Flow Vol 18, No 1, pp 123–140, 1992
Printed in Great Britain

0301-9322/92 $5.00 + 0.00

FLOW PATTERN TRANSITIONS IN TWO-PHASE LIQUID–LIQUID FLOW IN HORIZONTAL TUBES

N. BRAUNER and D. MOALEM MARON
Department of Fluid Mechanics and Heat Transfer, Faculty of Engineering, University of Tel-Aviv, Ramat-Aviv 69978, Tel-Aviv, Israel

(Received 2 April 1990; in revised form 5 August 1991)

Abstract—As the various concepts and results experienced in gas–liquid two-phase flows cannot readily be translated to liquid–liquid systems, an attempt is made to form a basis for constructing a general two-fluid flow pattern map. The departure from a steady stratified configuration to other bounding flow patterns is analysed in view of the relationships between the instability criterion and the conditions for reality of characteristics, which evolve from exploring the stability and well-posedness of the governing equations. The transitional boundaries between the other flow patterns encountered in liquid–liquid systems are obtained based on mechanistic models. A parametric study made for wide ranges of geometry and physical properties, as encountered in liquid–liquid systems, is also included. Comparisons of the proposed transitional criteria with (limited) available data in liquid–liquid systems show reasonable agreement. The convergence of the general criteria to the extremes of gas–liquid data, on the one hand, and the data of highly viscous core flows, on the other hand, is satisfactory.

Key Words liquid–liquid, oil–water, flow pattern transitions, stratified flow, core flow, stability

1. INTRODUCTION

Flows of mixtures of immiscible fluids are encountered frequently in the design of a variety of industrial processes and equipments. Gas–liquid two-phase flow represents a very particular "extreme" which has evoked extensive interest in the general area of multiphase flow in the last few decades. The resulting research into numerous aspects of various gas–liquid flows has contributed to a wide knowledge and understanding compared with that of other two-phase flows such as *liquid–liquid* mixtures. However, this in no way implies a lack of interest in the area of liquid–liquid flows. Depending on the flow conditions, liquid–liquid mixtures form various flow patterns of interest, some of which have been identified experimentally (Charles *et al.* 1961; Russell *et al.* 1959).

In principle, the behaviour of liquid–liquid two-phase flow is determined by the physical properties of the two layers, the system geometry and the associated flow pattern, as in gas–liquid mixtures. However, as has been shown recently by the authors (Brauner & Moalem Maron 1989, 1992; Brauner 1991), the various concepts and results experienced in gas–liquid two-phase flows cannot be readily translated to liquid–liquid flow predictions. Thus, with the lack of direct focus on the two-phase mechanisms associated with wide ranges of physical properties (density, viscosity and surface tension of the two fluids), the understanding of liquid–liquid two-phase flows remains inadequate.

A thorough analysis for each of the flow patterns is necessary in view of the different spatial distributions of the phases, which in turn determine the transport rates (momentum, heat and mass). Clearly, each of the flow patterns has its own particular practical interest. For instance, one of the aspects that attracts most attention is the reduction of pressure losses and power requirements in horizontal pipelines by the addition of a less viscous, immiscible liquid, as a second phase. The separate analyses of stratified (Brauner & Moalem Maron 1989) annular or highly viscous core flows (Moalem Maron *et al.* 1990; Brauner 1991) for wide ranges of tube size, viscosity and density ratios, show the regions with the best operational conditions for each flow pattern and their advantages. Moreover, the analyses of the various flow patterns shed some light on the possible mechanisms of transitions to others bounding flow patterns.

The present study proceeds along the following lines: analysing the various transitional criteria and parametrically studying the effects of the physical properties of the two fluids for wide ranges

of density and viscosity ratios, which are particularly important in liquid–liquid systems. The integration of the various transitional boundaries yields flow pattern maps for liquid–liquid systems which define the region of existence of the various patterns.

2. FLOW PATTERN TRANSITION CRITERIA

Referring to horizontal or slightly inclined flows, the simultaneous introduction of two immiscible fluids having a density differential is considered. For some limited range of relatively low fluid flow rates, the gravity forces due to the density difference are dominant and stratified flow is the natural resulting pattern.

2.1. Stratified flow boundaries

The transitions from smooth steady stratified flow to other (annular or intermittent) flow patterns in gas–liquid systems, have been commonly tackled by resorting to stability analyses (e.g. Lin & Hanratty 1986; Hanratty 1987), with some reference to the conditions for obtaining real characteristics (Banerjee 1985). In the accompanying paper, and as a prior phase to this work, the authors present a comprehensive study for the general liquid–liquid system on the relationship between stability criteria, and those for obtaining real characteristics, by exploring the well-posedness of the initial value hyperbolic set of the governing equations (Brauner & Moalem Maron 1992).

Utilizing the average one-dimensional two-fluids *transient* formulation, the resulting continuity equations for the two layers and combined momentum equations (figure 1) are:

$$\frac{\partial}{\partial t}(\rho_b A_b) + \frac{\partial}{\partial x}(\rho_b A_b u_b) = 0, \tag{1a}$$

$$\frac{\partial}{\partial t}(\rho_a A_a) + \frac{\partial}{\partial x}(\rho_a A_a u_a) = 0 \tag{1b}$$

and

$$\left[\rho_b(1-\gamma_b)\frac{u_b}{A_b} + \rho_a(1+\gamma_a)\frac{u_a}{A_a}\right]\frac{dA_b}{dh}\frac{\partial h}{\partial t} + (\rho_b - \rho_a)g\cos\beta\frac{\partial h}{\partial x} + \frac{(\partial P_{ib} - \partial P_{ia})}{\partial x} + \rho_b\frac{\partial u_b}{\partial t} + \rho_b\gamma_b u_b\frac{\partial u_b}{\partial x} - \rho_a\frac{\partial u_a}{\partial t} - \rho_a\gamma_a u_a\frac{\partial u_a}{\partial x} = \Delta f_{ba}, \tag{1c}$$

with

$$\Delta f_{ba} = \frac{-\tau_b S_b}{A_b} \pm \tau_i S_i\left(\frac{1}{A_b} + \frac{1}{A_a}\right) + \tau_a\frac{S_a}{A_a} + (\rho_b - \rho_a)g\sin\beta \tag{2a}$$

and

$$\frac{\partial}{\partial x}(P_{ib} - P_{ia}) = -\frac{\partial}{\partial x}\left\{\sigma\frac{\dfrac{\partial^2 h}{\partial x^2}}{\left[1 + \left(\dfrac{\partial h}{\partial x}\right)^2\right]^{\frac{3}{2}}}\right\}, \tag{2b}$$

where u_a, u_b and h are the instantaneous local values of the phase velocities and lower layer depth, A and S denote the flow cross-section and wetted perimeter and γ_a and γ_b are the shape factors which account for a velocity distribution in the two layers. The modelling of the various shear stresses terms in [2a] is detailed in Brauner & Moalem Maron (1992). Note that, "adjustable definitions" for the hydraulic diameters of the two phases (according to the relative velocity between the phases) has been adopted.

A temporal stability analysis carried out on the linearized form of [1, 2] yields the dispersion relation

$$aC^2 - 2(b_1 + ib_2)C + d_1 + id_2 = 0; \quad C \equiv \omega/k, \tag{3a}$$

and

$$C_{1,2} = \frac{1}{a}(b_1 + ib_2) \pm \frac{1}{a}[(b_1 + ib_2)^2 - a(d_1 + id_2)]^{\frac{1}{2}}, \tag{3b}$$

with

$$a = \rho_b \frac{A_b'}{A_b} + \rho_a \frac{A_b'}{A_b}; \quad A_b' = \frac{dA_b}{dh},$$

$$b_1 = \rho_b \frac{A_b'}{A_b} \gamma_b U_b + \rho_a \frac{A_b'}{A_b} \gamma_a U_a,$$

$$b_2 = \frac{1}{2k}\left(\frac{A_b'}{A_b}\frac{\partial \Delta F_{ab}}{\partial U_b} - \frac{A_b'}{A_b}\frac{\partial \Delta F_{ab}}{\partial U_a}\right),$$

$$d_1 = \rho_b \frac{A_b'}{A_b} \gamma_b U_b^2 + \rho_a \frac{A_b'}{A_a} \gamma_a U_a^2 - [(\rho_b - \rho_a) g \cos\beta + \sigma k^2]$$

and

$$d_2 = \frac{1}{k}\left(\frac{A_b'}{A_b} U_b \frac{\partial \Delta F_{ab}}{\partial U_b} - \frac{A_b'}{A_a} U_a \frac{\partial \Delta F_{ab}}{\partial U_a} - \frac{\partial \Delta F_{ab}}{\partial H}\right).$$

Here, C represents the complex propagation velocity of the disturbance, k is the wave number and $\partial \Delta F_{ab}/\partial(H, U_a, U_b)$ are $\partial f_{ab}/\partial(h, u_a, u_b)$ at steady conditions H, U_a, U_b. The neutral stability conditions are obtained by requiring the zero imaginary part for C, whereby [3a,b] yield:

$$C_{rn} = \frac{d_2}{2b_2} = \frac{\frac{\tilde{A}_b'}{\tilde{A}_b} U_b \frac{\partial \Delta F_{ab}}{\partial U_b} - \frac{\tilde{A}_b'}{\tilde{A}_a} U_a \frac{\partial \Delta F_{ab}}{\partial U_a} - \frac{\partial \Delta F_{ab}}{\partial \tilde{H}}}{\frac{\tilde{A}_b'}{\tilde{A}_b}\frac{\partial \Delta F_{ab}}{\partial U_b} - \frac{\tilde{A}_b'}{\tilde{A}_b}\frac{\partial \Delta F_{ab}}{\partial U_a}} \qquad [4]$$

and

$$\frac{\pi^2}{16 Dg \cos\beta}\left\{\frac{\rho_a}{\rho_b}\frac{\tilde{A}_b'}{\tilde{A}_a^3} U_{as}^2\left[\left(\frac{C_{rn}}{U_a} - 1\right)^2 + (\gamma_a - 1)\left(1 - 2\frac{C_{rn}}{U_a}\right)\right] + \frac{\tilde{A}_b'}{\tilde{A}_b^3} U_{bs}^2\left[\left(\frac{C_{rn}}{U_b} - 1\right)^2 + (\gamma_b - 1)\left(1 - 2\frac{C_{rn}}{U_b}\right)\right]\right\} - \left[\frac{(\rho_b - \rho_a)}{\rho_b} + \frac{\sigma k_n^2}{\rho_b g \cos\beta}\right] = 0. \qquad [5]$$

The non-dimensional form of [5] is

$$\frac{\varepsilon_b'}{1 - \varepsilon_b^3}\left[\left(\frac{C_{rn}}{U_a} - 1\right)^2 + (\gamma_a - 1)\left(1 - 2\frac{C_{rn}}{U_a}\right)\right] \mathrm{Fr}_a^2 + \frac{\varepsilon_b'}{\varepsilon_b^3}\left[\left(\frac{C_{rn}}{U_b} - 1\right)^2 + (\gamma_b - 1)\left(1 - 2\frac{C_{rn}}{U_a}\right)\right] \mathrm{Fr}_b^2 - (1 + \tilde{k}^2 \mathrm{We}_b \mathrm{Fr}_b^2) = 0, \qquad [6]$$

with

$$\mathrm{Fr}_a^2 = \frac{\rho_a}{\Delta\rho}\frac{U_{as}^2}{Dg\cos\beta}, \quad \mathrm{Fr}_b^2 = \frac{\rho_b}{\Delta\rho}\frac{U_{bs}^2}{Dg\cos\beta} = \frac{\rho_b}{\rho_a}\frac{\mathrm{Fr}_a^2}{\phi^2}, \quad \phi = \frac{U_{as}}{U_{bs}}, \quad \tilde{k} = kD,$$

$$\mathrm{We}_b = \frac{\sigma}{\rho_b D U_{bs}^2} = \frac{\rho_a}{\rho_b}\phi^2 \mathrm{We}_a, \quad \varepsilon_b = \frac{\tilde{A}_b}{\tilde{A}}, \quad \varepsilon_b' = \frac{d\varepsilon_b}{d\tilde{H}}; \qquad [7]$$

where ε_b denotes the lower phase hold-up and Fr_a, Fr_b, We_a and $\tilde{k}$ represents the Froude, Weber and non-dimensional wave numbers, respectively.

In parallel, the conditions under which the governing system [1a–c] constitutes a well-posed initial value problem, thus possessing real characteristics, have been shown to be

$$\tilde{\rho}_b U_b^2 \gamma_b(\gamma_b - 1) + \tilde{\rho}_a U_a^2 \gamma_a(\gamma_a - 1) - (\gamma_b U_b + \gamma_a U_a)^2 + \frac{D}{\rho_{ab}}[(\rho_b - \rho_a) g \cos\beta + \sigma k^2] \geq 0. \qquad [8a]$$

In its non-dimensional form [8a] reads

$$\tilde{\rho}_b \gamma_b(\gamma_b - 1)\left(\frac{\tilde{A}}{\tilde{A}_b}\right)^2 + \tilde{\rho}_a \gamma_a(\gamma_a - 1)\left(\frac{\tilde{A}}{\tilde{A}_a}\right)^2 \phi^2 - \left(\gamma_b \frac{\tilde{A}}{\tilde{A}_b} - \phi\gamma_a \frac{\tilde{A}}{\tilde{A}_a}\right)^2 + \mathrm{Fr}_{ab}^{-2} + \mathrm{We}_{ab}\tilde{k}^2 \geq 0, \qquad [8b]$$

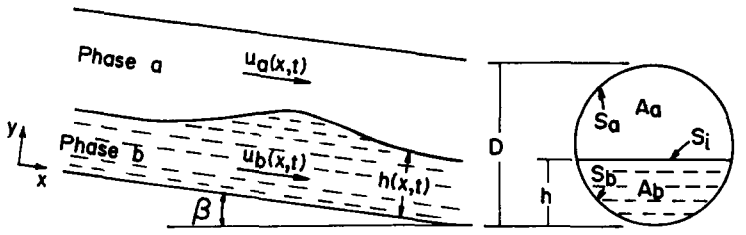

Figure 1 Schematic description of a stratified flow configuration

where

$$Fr_{ab} = \frac{\rho_{ab}}{\rho_b} Fr_b, \quad We_{ab} = \frac{\rho_b}{\rho_{ab}} We_b, \quad \tilde{\rho}_b = 1 + \frac{\rho_b}{\rho_a}\frac{\tilde{A}_a}{\tilde{A}_b}, \quad \tilde{\rho}_a = 1 + \frac{\rho_a}{\rho_b}\frac{\tilde{A}_b}{\tilde{A}_a}, \quad \rho_{ab} = \frac{\tilde{A}'_b}{\tilde{A}_a \tilde{A}_b}\frac{\rho_a \rho_b}{\frac{\rho_a}{\tilde{A}_a} + \frac{\rho_b}{\tilde{A}_b}}. \quad [8c]$$

The stability and well-posedness analyses were carried out around an assumed smooth stratified flow configuration. The solution for the fully-developed stratified flow (H, U_a, U_b) is detailed in Brauner & Moalem Maron (1989). The relation between the neutral stability conditions [4] and [5], the real characteristics condition [8] and the departure from the stratified flow configuration is shown in figures 2 and 3.

Figure 2 shows typical trends of the variation in amplification with the wave number [$C_i = \mathcal{I}m\{C\}$ vs k] in terms of (U_{as}, U_{bs}) combinations as calculated by [4] and [5]. For a certain set of (U_{as}, U_{bs}), as depicted by curve (a), there exists no wave number for which the amplification is positive. Thus, for the entire range of k (or wavelengths), all disturbances are expected to decay. On the other hand, for other combinations of (U_{as}, U_{bs}), as in curve (c), a smooth interfacial structure is maintained only for $k > k_n$ (or $\lambda < \lambda_n$). For $0 \leqslant k \leqslant k_n$, or sufficiently long waves, where the destabilizing effect of surface tension becomes small, the disturbances are amplified and hence, a wavy interfacial structure develops. Depending on the (U_{as}, U_{bs}) set, the range of amplified waves, $0 < k < k_n$, may be reduced. For particular combinations of (U_{as}, U_{bs}), as represented by curve (b),

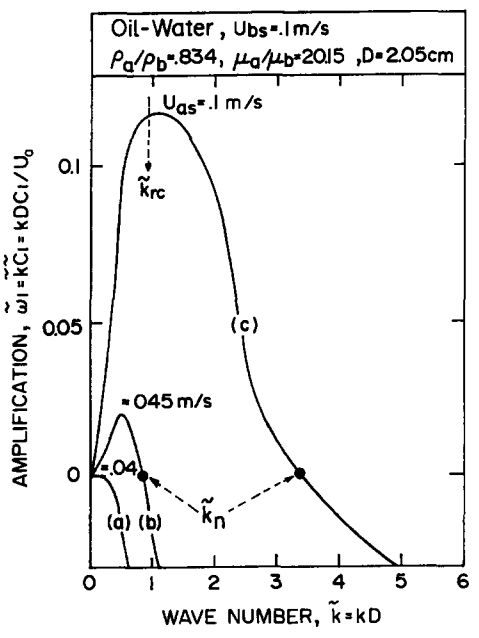

Figure 2 Amplification vs wave number. range of unstable modes.

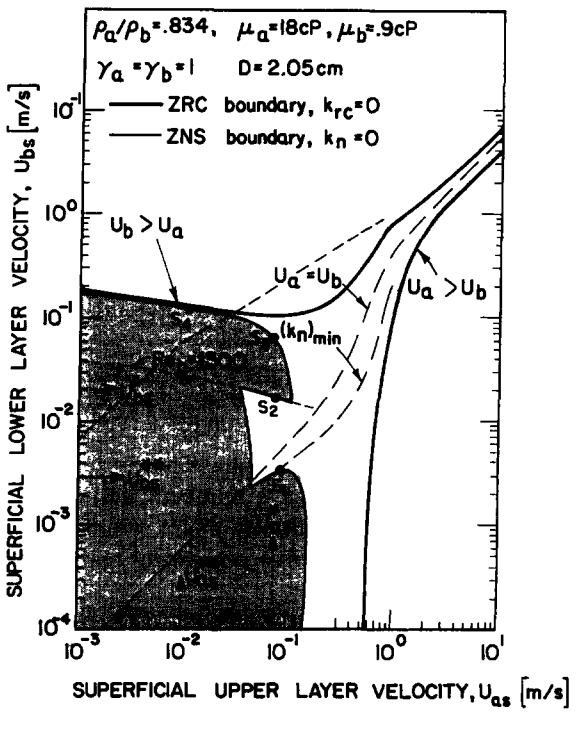

Figure 3 ZNS and ZRC boundaries for an oil–water system

the amplified range diminishes. In searching for all combinations of (U_{as}, U_{bs}) for which $k_n \to 0$, the "*zero neutral stability*" (ZNS) line in figure 3 is obtained. This boundary confines all possible smooth stratified flows. The locus of the curve itself represents the departure from the smooth stratified structure. For any operational set (U_{as}, U_{bs}), outside the $k_n = 0$ boundary, the linear stability analysis predicts exponential growth with time for a finite range of wave numbers, $0 \leqslant k \leqslant k_n$. The growth of disturbances in this region may either be damped (due to non-linear effects) and thus end with "stable wavy" stratified flow, or may result in a different flow configuration (due to bridging, for instance).

Also indicated on curve (c) of figure 2 is the minimum wave number, k_{rc}, which ensures real characteristics. This is obtained by [8] for a given set of (U_{as}, U_{bs}). Thus, for all $k < k_{rc}$, an unstable stratified flow is consistently predicted by both stability and well-posedness analyses. However, for $k_{rc} < k < k_n$, while the governing equations [1a–c] are well-posed, they are still expected to develop a wavy structure (according to stability analysis). As is shown by the authors elsewhere (Brauner & Moalem Maron 1992), the value of k_{rc} is always within the amplified range, $k_{rc} \leqslant k_n$.

In parallel with the physical interpretations of the ZNS boundary given above, defined by $k_n = 0$, an analogue boundary is constructed by searching for all combinations of (U_{as}, U_{bs}) which yield real characteristics for $k_{rc} = 0$ (by [8a,b]). The "*zero real characteristics*" (ZRC) boundary is included in figure 3 and is shown to fall away from the previous ZNS boundary, in the region where no stable smooth stratified flow is expected to exist. As demonstrated in figure 3, the ZRC boundary is composed of two branches; the upper one corresponds to $U_b > U_a$, while along the side branch $U_a > U_b$. The two branches approach one another in the region of high velocities of both phases, U_a and U_b, where the difference in the two is just sufficient to balance the gravity term in [8a]. As these two branches get closer, a double solution is obtained (for either specified U_{as} or U_{bs}). Thus, at relatively high velocities, there exists a narrow range of operational conditions for which real characteristics are still ensured. The location of this region and its width depend mainly on the density differential.

It is of interest to elucidate the non-monotonous behaviour of the ZNS boundary. Here too, multiple solutions are obtained for $k_n = 0$ while searching for U_{as} at constant U_{bs} and vice versa. For instance, increasing U_{bs} along U_{as}^*, the first solution S_1 is obtained, beyond which an amplified wavy zone is predicted that extends to point S_2. Up to point S_2, laminar flow of phase b is maintained. At point S_2, phase b becomes turbulent ($Re_b = Re_{cr} = 1500$) and [3a,b] and [5] for turbulent phase b predict again stable smooth flow (all modes are damped by [3a,b] and no physical solution for $k_n \geqslant 0$ by [5]). For clarity, the transitional line from laminar to turbulent phase b is also indicated in figure 3. The transition from stable to unstable stratified flow, which takes place along the laminar/turbulent boundary is thus discontinuous. With a further increase in U_{bs}, another solution S_3 for $k_n = 0$ is now obtained with phase b turbulent. Note that, for low $U_{as} = U_{as}^{**}$, the laminar flow of phase b always remains stable, while the turbulent becomes unstable at point S_4, whereby a single solution (for $k_n = 0$) is obtained.

Similarly, for constant $U_{bs}^* \simeq 2$ cm/s, three transitions are obtained, one of which is again discontinuous due to the laminar/turbulent transition. However, at low $U_{bs}^{**} \simeq 0.3$ cm/s, the various transitions are due to multiple solutions of [5] obtained for laminar flows in both phases.

Also included in figure 3 is the locus of (U_{as}, U_{bs}) which corresponds to a local minimum of the neutral stable wave number in the amplified zone ($k_n > 0$). Clearly, around the $(k_n)_{min}$ line, the range of amplified modes $0 < k < (k_n)_{min}$ is relatively narrow and is continuously reduced as this line approaches the stable smooth boundary (around S_1). When $(k_n)_{min} = 0$ the stable/unstable boundary is crossed.

The general outcome of the ZNS and ZRC lines is to define three zones; the area below the ZNS boundary, is well-understood to be the stable smooth stratified zone. In the "*buffer*" zone between the two boundaries, though amplified interfacial waves exist, the equations which govern the variation of (h, u_a, u_b) in space and time are still well-posed with respect to all unstable modes. Beyond the ZRC boundary the complex characteristics imply that the governing equation for the stratified flow configuration cannot accomodate the time and space variation associated with a certain range of amplified wave modes. Thus, while the ZNS boundary may represent a preliminary transition to a wavy interfacial structure, the ZRC boundary, which is well-advanced in the wavy

unstable region, represents an upper bound for the existence of a wavy stratified configuration, beyond which another flow pattern prevails.

In view of the implications to flow pattern transitions associated with the ZNS and ZRC boundaries, it is of interest to demonstrate these boundaries for various liquid–liquid systems. As figure 3 relates to a particular system ($\rho_a/\rho_b = 0.834$, $\mu_a/\mu_b \simeq 20$), figures 4–7 summarize the effects of density and viscosity ratios, shape factors and conduit diameter.

Figure 4 indicates that as the density differential decreases, the stable smooth stratified zone (confined by the ZNS line) is reduced, thus a stable smooth stratified flow pattern is maintained in a limited range of operational conditions (U_{as}, U_{bs}) [figures 4(a,b)]. Similarly, as the viscosity ratio increases, the velocity gap between the phases tends to increase, leading to a more limited zone for stable smooth stratified flow [figures 4(b,c)]. In general, the range for well-posedness (as confined by the ZRC lines) is also reduced by either decreasing the density differential or increasing the viscosity gap.

It is interesting to refer at this point to the effects of the shape factor, as demonstrated in figures 4(a–c). As [8a] indicates, for $\gamma_a, \gamma_b > 1$ additional stabilizing terms result. Thus, inclusion of the shape factors may extend the region of operational conditions for which real characteristics are obtained. A shape factor > 1 is more likely in laminar (viscous) layers. As in liquid–liquid system, the lighter phase is usually also the more viscous one (oil–water systems), the effect of γ_a is demonstrated in figures 4(a–c). It is shown that for a given oil flow rate, U_{as}, well-posedness is ensured at a higher water rate, U_{bs}, as the oil shape factor, γ_a, increases. Note that the effect of the oil shape factor, γ_a, is demonstrated with respect to the upper branch along which $U_b > U_a$, whereas along the side branch, where $U_a > U_b$, a shape factor of 1 may reasonably be assumed for the (high velocity) viscous phase as well. Inspection of [5] indicates that the inclusion of the shape factors in the stability analysis may contribute additional stabilizing terms (for $C_m/U_a > 0.5$ or $C_m/U_b > 0.5$), in which case the range for stable smooth stratified flow is also extended.

As the ZRC boundaries are interpreted as the upper limits for maintaining a stratified flow configuration, further illustrations of the effects of physical properties and system geometry on the ZRC boundaries are detailed in figures 5–7. Again, for liquid–liquid systems of greater density

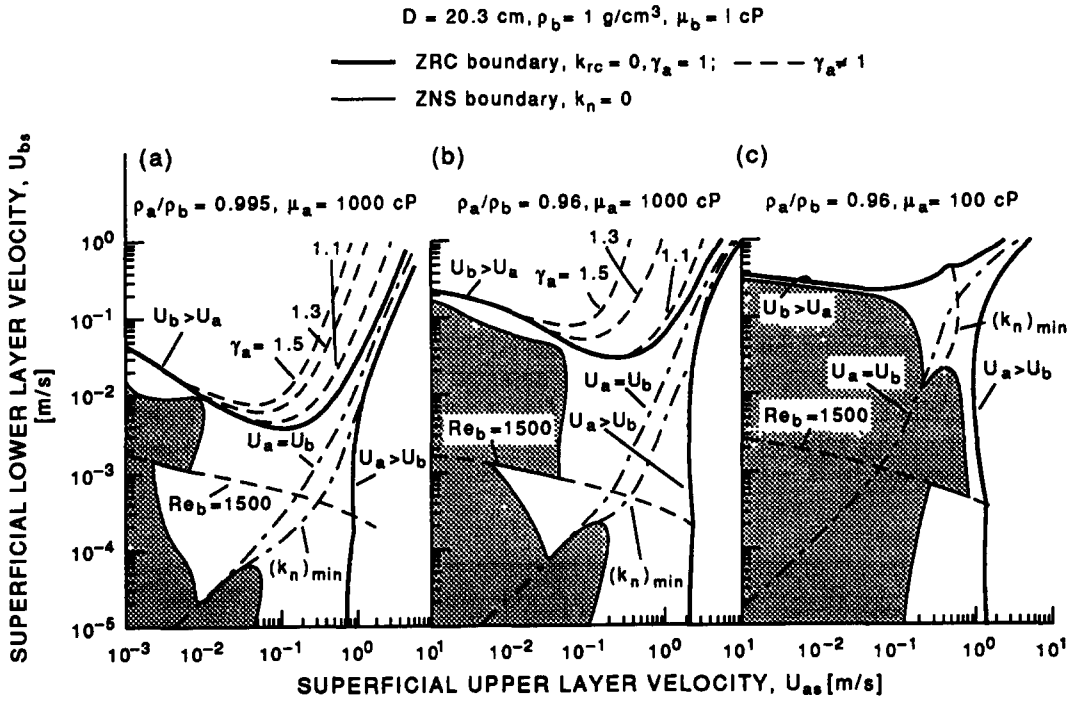

Figure 4. The effect of the density differential and the viscosity ratio on the locations of the ZNS and ZRC boundaries.

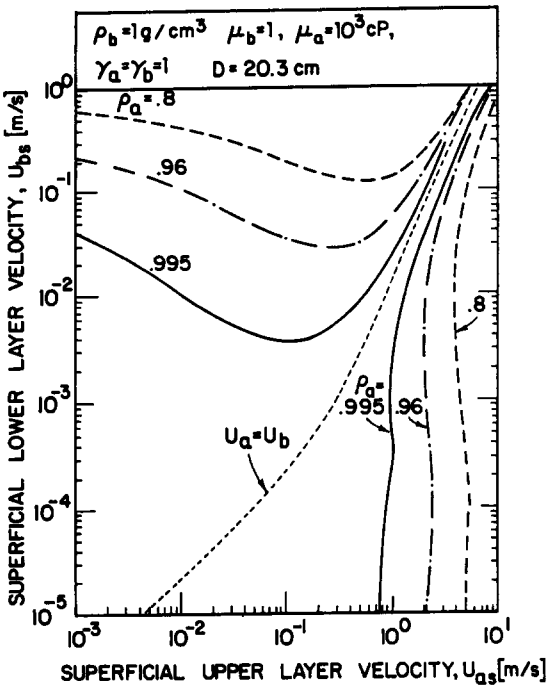

Figure 5 The effect of the density differential on the ZRC boundary.

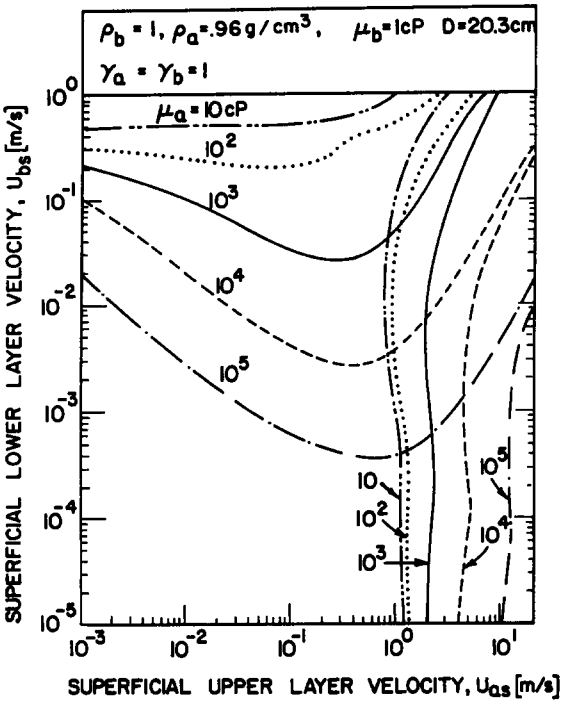

Figure 6 The effect of the viscosity ratio on the ZRC boundary.

difference, wider ranges of both oil and water flow rates may sustain a stratified flow pattern (figure 5). Whereas, with an increasing viscosity gap, the departure from the stratified flow pattern occurs consistently at lower water ratios (the water rate is reduced for a given oil rate along the upper branch or the oil rate increases for a given water rate along the side branch). It is particularly interesting to note that for a given oil viscosity there exists an extremal oil rate for maintaining a stratified pattern, which is almost independent of the water rate. This extremal value (location of the side branch) increases with oil viscosity. On the other hand, for high-viscous oils, the analysis predicts that a certain oil flow rate exists for which the water rate required to cause departure from stratified flow is minimal (along the upper branch). This minimum water ratio decreases with oil viscosity. The above observations have practical implications with regard to high viscous core flow performance, as is discussed below.

Figure 7 represents the effects of tube diameter on the range of the stratified flow configuration, whereby higher water and oil rates (along the upper and side branches, respectively) are required for transitions with increasing tube diameter. Clearly, the extended ranges of the operational rates (U_{as}, U_{bs}) for maintaining a stratified pattern at higher diameters, adversely affect the possibility of other flow patterns developing.

The construction of the *complete* stratified/non-stratified transitional boundary based on integrated considerations of stability and well-posedness are proposed and examined in section 3 in view of the experimental data for various two-fluid systems.

2.2. Annular flow boundaries

In order to determine whether an annular pattern collapses into stratified or slug flows, the modelling of annular flow is required. Recently, Brauner (1990) presented a physical model for annular liquid–liquid systems (figure 8). The model encompasses within a common framework all possible flow situations of laminar–laminar, turbulent–turbulent and mixed flow regimes in the two phases for wide ranges of physical properties (viscosity and density), and yields the core phase diameter, D_c (or *in situ* hold-up, ε_a), and the corresponding pressure drop. For the common case of a laminar viscous oil core, with either a laminar or turbulent annular (water) phase, simple

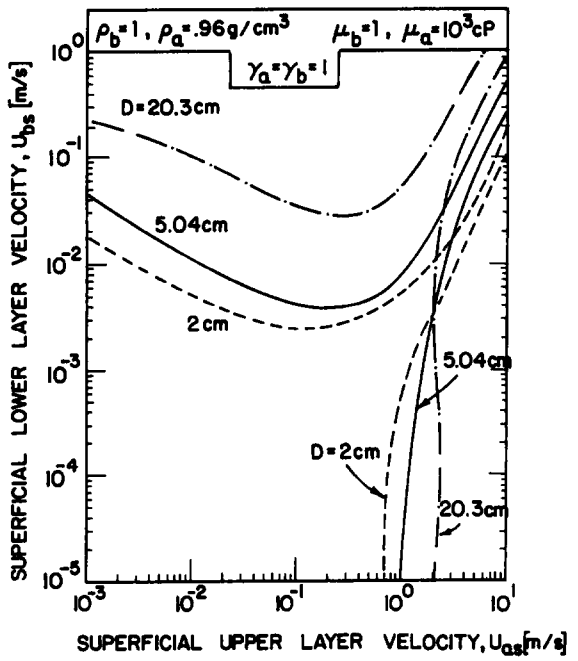

Figure 7. The effect of the tube diameter on the ZRC boundary

explicit solutions for D_c have been obtained. For a laminar core–laminar annular layer, L–L (see also Russell & Charles 1959),

$$\tilde{D}_c = \left\{ \frac{\phi}{\left[\frac{1}{B}\frac{\mu_w}{\mu_c}\phi\frac{G(\phi)}{F(\phi)}\right]^{\frac{1}{2}} + \phi + \frac{G(\phi)}{F(\phi)}} \right\}^{\frac{1}{2}}, \quad \varepsilon_a = (1-\tilde{D}_c^2)(1-\alpha_w) + \tilde{D}_c^2\alpha_c, \qquad [9a]$$

where

$$F(\phi) = \frac{[\alpha_w\phi - (1-\alpha_w)]}{\phi[\alpha_c + \alpha_w - 1]}, \quad G(\phi) = \frac{[\alpha_c - (1-\alpha_c)\phi]}{[\alpha_c + \alpha_w - 1]}, \quad \tilde{D}_c = \frac{D_c}{D};$$

and for a laminar core–turbulent annular layer, L–T,

$$\tilde{D}_c = \left\{ \frac{\phi}{\chi\phi\left[\frac{1}{B}\frac{\mu_a}{\mu_c}\frac{\rho_w}{\rho_b}\left(\frac{\nu_w}{\nu_b}\right)^{0.2}\frac{G(\phi)^{1.8}}{F(\phi)}\right]^{\frac{1}{2}} + \phi + \frac{G(\phi)}{F(\phi)}} \right\}^{\frac{1}{2}}, \qquad [9b]$$

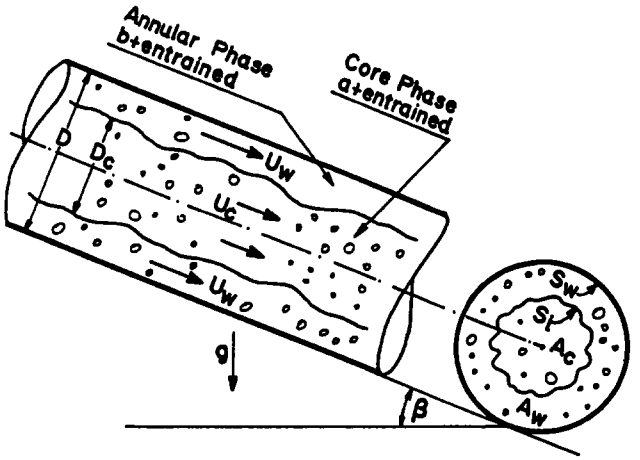

Figure 8. Schematic description of an annular flow configuration.

where

$$\chi^2 = \frac{0.046}{16}\frac{\mu_b}{\mu_a}\frac{1}{\phi}(\mathrm{Re}_{bs})^{0.8} = \frac{0.046}{16}\left(\frac{\mu_b}{\mu_a}\right)^{0.2}\left(\frac{\rho_b}{\rho_a}\right)^{0.8}\frac{1}{\phi^{1.8}}\mathrm{Re}_{as}^{0.8};$$

$$\rho_c = \rho_a\alpha_c + \rho_b(1-\alpha_c), \quad \alpha_c = \frac{A_{ac}}{A_c}; \quad \rho_w = \rho_b\alpha_w + \rho_a(1-\alpha_w), \quad \alpha_w = \frac{A_{bw}}{A_w}; \qquad [9c]$$

Re_{as} and Re_{bs} are the superficial Reynolds numbers, B is an augmentation factor of the interfacial shear stress due to waviness, A_c, A_w, ρ_c and ρ_w are the areas and equivalent densities of the core and annular wall phases due to entrainment of $(1-\alpha_c)$ of phase b into the core and $(1-\alpha_w)$ of phase a into the wall phase. For pure core phase a and pure annular phase b, $\alpha_c = \alpha_w = 1$.

A transition criterion is derived now by looking for the limiting situation of an annular configuration. In the range where stable annular flow has been observed, it has been found that $A_w/A \ll 1$, which corresponds to a relatively thin annular layer. Increasing the annular phase flow rate, U_{bs}, yields a thicker wavy annular layer. With a sufficiently thick annular layer, the growing interfacial waves may block the core space leading to the formation of oil slugs and bubbles. This mechanism of core disintegration evolves from the inherent Rayleigh instability associated with a moving cylindrical jet, well-known in reference to free-liquid jets. However, in annular flow, further complications due to the damping effects of the conduit wall on the eccentric core are to be accounted for. Instead, a rather realistic transitional criterion may be established by exploring the critical *in situ* hold-up, which generates favourable conditions for the growing interfacial waves to reach the core centre.

A transition line to a slug pattern is established by searching for those (U_{as}, U_{bs}) for which the annular model equations fulfil a prescribed criterion, such as either $D_c \simeq D/2$ or $A_c \simeq A_w \simeq A/2$. For the particular case of a viscous laminar core, either of the explicit expressions in [9a,b] are used, and when the requirement of $A_w \simeq A/2$ ($\tilde{D}_c = \sqrt{2}/2$) is used for instance (with $B = 1$), the criterion for the annular/slug transition reads:

$$\left[\frac{\mu_w}{\mu_c}\phi\frac{G(\phi)}{F(\phi)}\right]^{\frac{1}{2}} + \frac{G(\phi)}{F(\phi)} - \phi \geqslant 0 \qquad \text{L–L;} \qquad [10a]$$

and

$$\chi\phi\left[\frac{\mu_a}{\mu_c}\frac{\rho_w}{\rho_b}\left(\frac{v_w}{v_b}\right)^{0.2}\frac{G(\phi)^{1.8}}{F(\phi)}\right]^{\frac{1}{2}} + \frac{G(\phi)}{F(\phi)} - \phi \geqslant 0 \qquad \text{L–T.} \qquad [10b]$$

In the absence of entrainment, $\alpha_c = \alpha_w = 1$, and [10a,b] reduce to

$$\left[\frac{\mu_b}{\mu_a}\phi\right]^{\frac{1}{2}} - \phi + 1 \geqslant 0 \qquad \text{L–L} \qquad [11a]$$

and

$$\chi\phi - \phi + 1 \geqslant 0 \qquad \text{L–T.} \qquad [11b]$$

For the case of a turbulent core phase (with either a laminar or turbulent annular layer) the implicit solution for $\tilde{D}_c$ (Brauner 1991) is to be employed.

Figures 9(a–c) demonstrate a parametric study on the predicted transition boundary from an annular to a slug pattern in various liquid–liquid systems. As indicated in figures 9(a–c), the effects of various parameters on this transition line in the studied ranges are rather mild: the tube diameter and density ratio have almost no effect, and oil viscosity has only a slight effect. This is understandable in view of [9a–c] and [10a,b], where for a laminar core (as in highly viscous oils), the *in situ* hold-up and hence the resulting transitional conditions are practically independent of the core viscosity. This is consistent with experimental data on viscous core flows (Oliemans 1986; Brauner 1991). In this case, the transitional line [11a,b] reduces to $\phi = U_{as}/U_{bs} \simeq 1$.

Note that figures 9(a,b) are based on $A_w/A_c = 1$ and $\alpha_c = 1$. The sensitivity of the annular/slug (AN–SL) transition line to these parameters is demonstrated in figure 9(c). The line obtained with $\alpha_c = 1$, $D_c/D = 0.5$ ($A_w/A_c = 3$) corresponds practically to an alternative transition line predicted with $\alpha_c = 0.5$, $A_w/A_c = 1$ ($D_c/D = \sqrt{2}/2$). Since at relatively high oil and water rates, entrainment of the less viscous annular layer may take place ($\alpha_c < 1$), a criterion of $A_w/A_c > 1$ with $\alpha_c = 1$ may

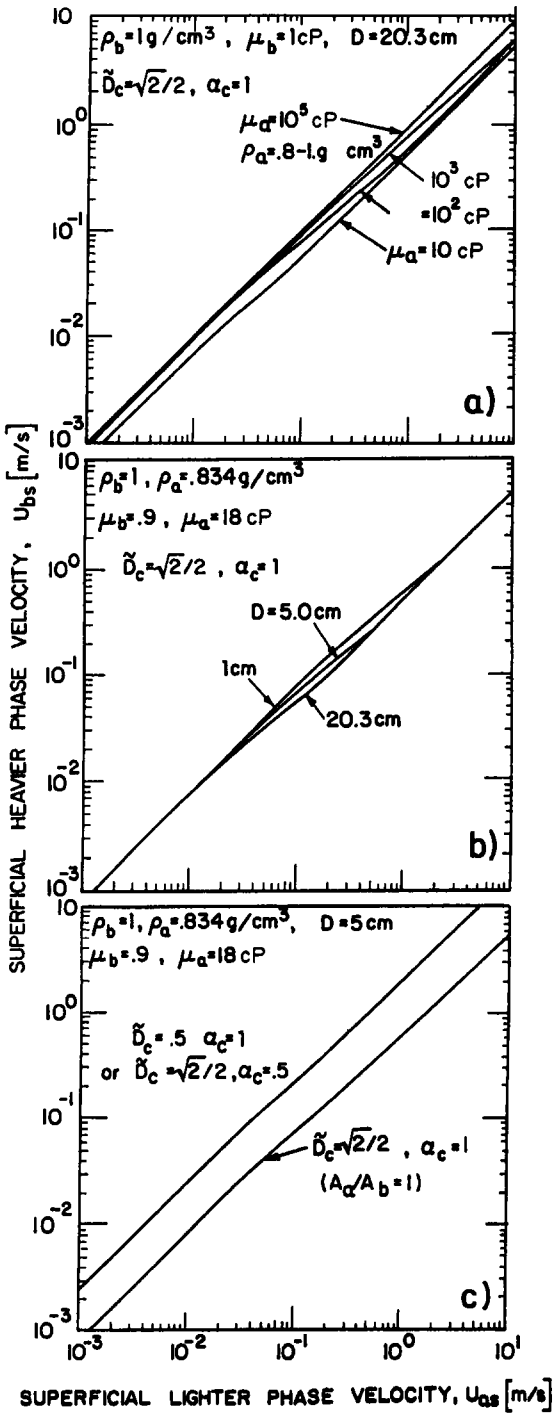

Figure 9. Effects of the liquids' physical properties, the tube diameter and model parameters on the AN–SL transition boundary.

compensate for ignoring entrainment. Clearly, the relevant criterion around $A_w/A_c \simeq 1$ is to be determined by comparison with experimental data (see also figure 14).

It is worth noting that the annular pattern is bounded, in fact, between two limits. While the above discussion relates to the collapse of the core phase in the case of a relatively thick (wavy) annular layer, the other limit relates to the break-up of the thin top-wall film due to the float-up tendency of the lighter core phase. In this case, the disruption of the annular configuration results

in a stratified pattern. This boundary is predicted via the analysis of the limit of existence of the stratified configuration (as described in section 2.1).

2.3. Stratified–dispersed/stratified boundary

Gas–liquid systems are known to stratify even for relatively low gas flow rates, due to the intense float-up of the bubbles and consequent accumulation of gas at the upper tube cross-section. When the density differential is reduced, as in liquid–liquid systems, buoyancy is moderated and the system tends to demonstrate a stratified–dispersed flow pattern, as sketched in figure 10. In order to develop a criterion for predicting whether the lighter phase, a, may form a continuous upper layer or remain above phase b as a swarm of drops, an initially very low U_{as}/U_{bs} ratio (where stable stratification is predicted as in section 2.1) is considered. Clearly, under the condition of sufficiently low U_{as}, drops (or bubbles) of phase a are obtained. In this range, the small viscous and inertia forces are insufficient to cause coalescence or avoid float-up of the bubbles. Thus, drops of the lighter phase a agglomerate at the upper cross-section due to buoyancy (corresponding to $\Delta\rho$) and tend to stick together. However, the drops may maintain their shape (provided they are small enough), so that the surface tension forces overcome those due to buoyancy, the balance of which yields the critical diameter, d_{cr}:

$$\sigma\pi d_{cr} = \tfrac{4}{3}\pi\left(\frac{d_{cr}}{2}\right)^3(\rho_b - \rho_a)g; \quad d_{cr} = \left[\frac{6\sigma}{(\rho_b - \rho_a)}g\right]^{\frac{1}{2}}. \qquad [12]$$

Equation [12] implies that drops of larger diameters will merge together to form a continuous upper layer.

For a given (U_{as}, U_{bs}) in the range of stable stratified flow, the stratified model is applied now, whereby the upper phase height, $H_a = D - H$, and its corresponding cross-sectional area, A_a, are obtained. Consider the case where $H_a \ll d_{cr}$, corresponding to relatively low U_{as}. In this case the biggest drop which may occupy the available space A_a is still smaller than d_{cr}. Therefore, a swarm of bubbles smaller than d_{cr} will be maintained within A_a, and a stratified-dispersed flow pattern is possible. On the other hand, for $H_a \gg d_{cr}$, corresponding to a greater upper phase flow rate, the available upper phase space allows the agglomeration of large drops, beyond the critical diameter, which will then merge to form an upper continuous stratified phase.

In view of the above, a simple transition criterion from two continuous stratified layers towards a stratified-dispersed upper layer is proposed herein, by requiring that for given (U_{as}, U_{bs}) flow

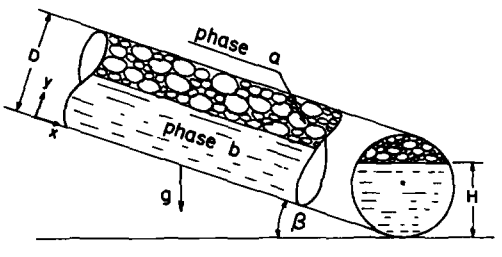

Figure 10 Schematic description of a stratified–dispersed flow configuration.

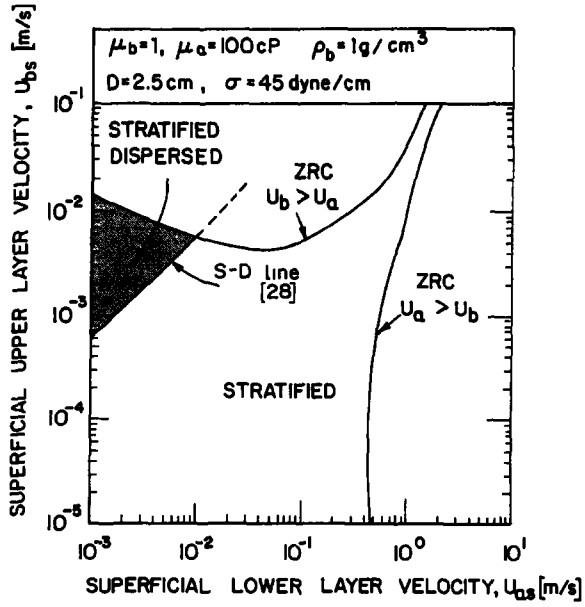

Figure 11. A stratified–dispersed configuration as a subzone of a continuous stratified configuration

rates, the available upper cross-sectional area, A_a, is smaller than the cross-sectional area of a critical drop size:

$$A_a(U_{as}, U_{bs}, \rho_a, \rho_b, \mu_a, \mu_b) \leqslant A_{cr}; \quad A_{cr} = \frac{\pi d_{cr}^2}{4}. \qquad [13]$$

Figure 11 shows the possible development of a dispersed upper layer as a subzone of the stratified configuration. Clearly, the only practical relevance of the S–D (stratified–dispersed) line is when it merges into the region where stable stratification is predicted. The shaded area represents the predicted zone of the stratified–dispersed pattern as a subzone of the stratified pattern. For generality, it is of interest to discuss the effects of the various physical properties and geometry on the S–D transition line, as detailed in figures 12(a–c).

With reference to [12], as $\Delta\rho$ increases, the critical diameter decreases, and thus a dispersed upper layer may result for a very low lighter phase flow rate. For example, in the extreme case of gas–liquid flow, [12] yields $d_{cr} = 0.6$ cm and [13] for $D = 5$ cm requires an air/water flow ratio of $\phi < 0.03$, which is out of the practical range of interest. Therefore, stratified–dispersed air–water flow has not been reported for $D = 5$ cm. It is worth noting, however, that as the upper layer becomes dispersed [as for small diameters, see figure 12(c)], usually it has been identified as an intermittent pattern (or bubbly flow). Therefore, the S–D transition is actually part of the observed stratified/intermittent transitional boundary.

Reducing the density differential (as in liquid–liquid systems) or increasing the surface tension, see figure 12(a), yields a larger critical drop diameter, whereby the dispersed upper layer can be sustained at larger A_a (corresponding to larger U_{as}). This may result in an extended dispersed zone (S–D line becomes lower). Note that the entire zone of stable stratification is also reduced with a decreasing density difference, as discussed in reference to figures 4 and 5.

The effect of the viscosity ratio is shown in figure 12(b). Increasing the viscosity of the upper layer affects larger A_a (for given flow rates and d_{cr}) and as long as $A_a > A_{cr}$ continuous stratified layers are maintained (S–D line moves upward). For sufficiently high μ_a/μ_b, the S–D line may not intersect the stratified ZRC line. It is to be noted in view of figures 6 and 12(b) that while the S–D lines move upward with increasing upper layer viscosity, the upper bound for stratification (ZRC line) moves downward, hence the existence of this stratified–dispersed subzone is less favourable in highly viscous oil systems. Similarly, as the tube diameter decreases, as in figure 12(c), the available space for the upper layer, A_a, becomes smaller (at given flow rates) and as $A_a < A_{cr}$ the stratified–dispersed pattern is more likely to appear according to the possible intersection with the corresponding ZRC (figure 7).

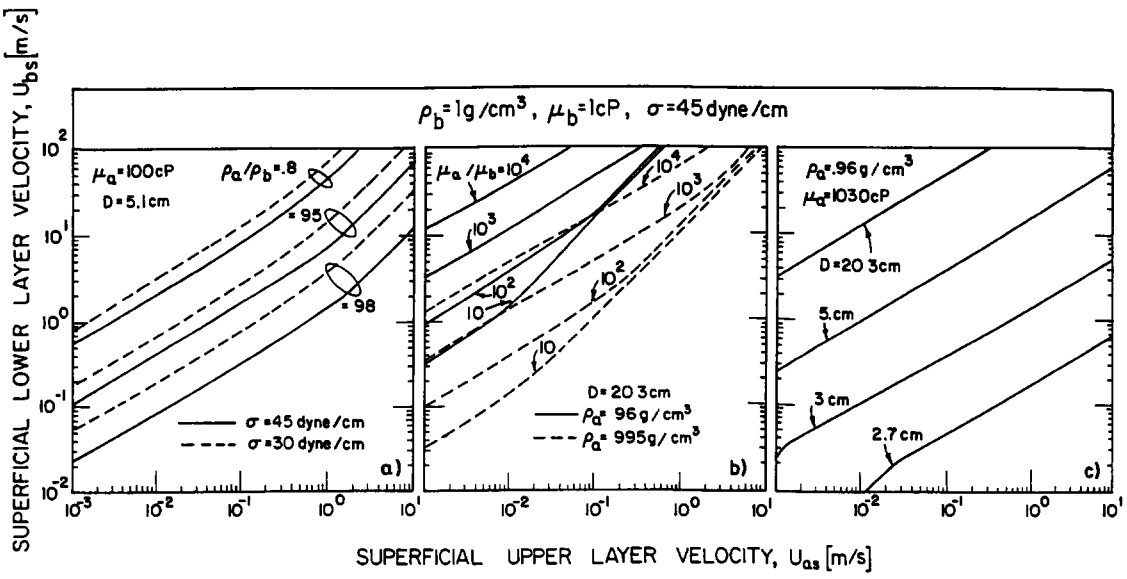

Figure 12 Effects of the liquids' physical properties and the tube diameter on the stratified/stratified–dispersed boundary

In the extreme case of equal densities, it is most likely that no stratification takes place and a dispersed flow pattern occupies the entire tube cross-section. The stratification may also disappear for a finite non-zero density differential, $\Delta\rho_{min}$, which is sufficiently low to yield (by [12]) a d_{cr} of the order of the tube diameter. For example, with reference to figure 12(c), $\Delta\rho = 0.04$ g/cm^3 (and $\sigma = 45$ dyne/cm) yields $d_{cr} = 2.65$ cm and therefore no stratified flow is to be expected for tube diameters smaller than $D_{cr} = 2.65$ cm, although the density difference between the layers is finite and a range of stable stratification is predicted by stability analysis. Stated differently, for a given tube diameter the whole range of $0 < \Delta\rho < \Delta\rho_{min}$, is expected to yield a dispersed flow and effectively behaves as an equal-density or zero-gravity system (Brauner 1990). The non-dimensional criterion for defining an apparently "*equal-density*" (or "*zero-gravity*") system is $d_{cr}/D > 1$, or in terms of the Eotvös number, Σ:

$$\Sigma \geqslant 1; \quad \Sigma = \frac{6\sigma}{\Delta\rho D^2 g}. \qquad [14]$$

The above discussion refers to the possibility of dispersed phase a in phase b for relatively low U_{as}. A similar reasoning can be adopted for the case of dispersed (heavier) phase b in phase a, when $U_{bs} \ll U_{as}$, whereby a dispersed pattern of the heavier phase may appear at the conduit bottom. In any case the appearance of a stratified–dispersed pattern may also depend on the interaction of the fluids with the pipe walls (Hasson *et al.* 1970).

2.4. Fully-dispersed pattern boundary

As discussed above, a stratified–dispersed pattern is relevant only when [13] merges into the ZRC boundary. However, beyond the ZRC boundary various dispersed types of flow may exist. For instance, above and close to the upper ZRC branch, when U_{bs} is large compared to U_{as} ($\phi \ll 1$), relatively large oil bubbles ($d > d_{cr}$) dispersed in water may be obtained. With increasing U_{as}, the oil bubbles merge to form large elongated oil bubbles which resemble slug flow. On the other hand, increasing U_{bs} while maintaining low U_{as}, the turbulent breakage forces tend to destroy large bubbles. According to Hinze's (1955) model, originally developed for liquid–liquid dispersion, the maximum dispersed phase diameter is related to the turbulent dissipation scale, l_d, by:

$$d_m = C_1(\varepsilon_a) l_d^{\frac{2}{5}} \left(\frac{\sigma}{\rho_b}\right)^{\frac{3}{5}}, \quad l_d = \frac{2fU^3}{D}; \qquad [15a]$$

and

$$U = U_m = U_{as} + U_{bs}, \quad f = 0.046\left(\frac{DU_m}{\nu_b}\right)^{-0.2}, \quad \varepsilon_a = \frac{U_{as}}{U_{as} + U_{bs}}; \qquad [15b]$$

where the constant $C_1(\varepsilon)$ may generally be related to the *in situ* hold-up and is to be determined by experiments [e.g. Hinze (1955) obtained $C = 0.725$ in a Couette flow field]. Utilizing [15b] in [15a] yields

$$\frac{d_m}{d_{cr}} = C_2(\varepsilon) We_m^{0.1} Fr_m^{-0.5} Re_m^{0.08}, \qquad [16a]$$

where

$$We_m = \frac{\sigma}{D\rho_b U_m^2}, \quad Fr_m = \frac{\rho_b U_m^2}{\Delta\rho g D}, \quad Re_m = \frac{DU_m}{\nu_b} \qquad [16b]$$

and with d_{cr} as given in [12]. Obviously, as the maximum drop size, d_m, is smaller than the critical size, d_{cr}, the small drops maintain their identity and a fully-dispersed pattern may prevail. Thus, a fully-dispersed pattern is expected for $d_m/d_{cr} < 1$ and $\phi \ll 1$, whereas for $\phi \approx 1$ ($\varepsilon_a \simeq 0.5$) (large *in situ* hold-up) a slug pattern may still be more favourable, even for $d_m/d_{cr} < 1$, due to the dense bubble packing. Note that for large U_{as} and relatively low U_{bs}, *fully-dispersed* phase b in continuous phase a, may be obtained (similar to the mist pattern in gas–liquid systems).

The various types of dispersed flow have been identified in liquid–liquid systems (Russell *et al.* 1959; Charles *et al.* 1961; Hasson *et al.* 1970). However, the exact location of the transitional boundaries are not well-defined (as in gas–liquid systems), probably due to the low density differentials. More extensive experimental data is required for thorough interpretations.

3. LIQUID–LIQUID FLOW PATTERN MAPS: COMPARISON WITH EXPERIMENTS

The parametric study presented so far forms the basis for constructing complete flow pattern maps for two various two–fluid systems. Clearly, the physical concepts utilized in developing the transitional boundaries ought to be supported by experimental observations. However, the available experimental data on liquid–liquid flow patterns is rather limited.

Figures 13 and 14(a,b) demonstrate comparisons of the predicted transitional boundaries with two horizontal oil–water systems: the first corresponds to $\mu_a = 18$ cP, $\rho_a = 0.834$ g/cm^3, $D = 2.05$ cm $\mu_b \equiv \mu_w = 0.894$ cP (Russell *et al.* 1959); and the second corresponds to a waxy oil–water system with $\mu_a = 10^4$ cP, $\rho_a = 0.995$ g/cm^3, $D = 20.3$ cm. (Guevara *et al.* 1988). Included in the figures are the upper ZRC branches obtained for various $\gamma_a \geqslant 1$ values. As noted earlier, $\gamma_a = 1$ corresponds to relatively high oil rates, while for lower oil rates $\gamma_a > 1$ is more suitable. Only the transitional data of stratified–dispersed and stratified–annular (which confine the stratified flow data) is indicated in figure 13. The data for a stratified pattern (not shown in the figure) is indeed confined by the combined boundaries formed by the two ZRC branches and the S–D transition line. The transitional stratified–dispersed data follows the predicted S–D boundary. Similarly, the data corresponding to the transition to annular pattern data is located in the proximity of the ZRC side branch, $U_a > U_b$. Note that the ZNS line for the oil–water system of figure 13 seems to be irrelevant to transition.

Figure 14(a) includes specific data which relates to annular (viscous) core flow. The region where core flow has been steadily maintained (Guevara *et al.* 1988) is indeed located in the predicted region for an annular pattern (confined between the AN–SL boundary and the upper ZRC branch with $\gamma_a \simeq 1$ to 1.1). As shown in figure 14(a), no data (of core flow conditions) falls across the AN–SL transition line. Note that for the particular physical system of figure 14(a), the S–D line does not share a common zone with the stratified region, thus no stratified–dispersed pattern is expected in this case.

The upper ZRC boundary of figure 14(a) as well as the core flow data are reconstructed in figure 14(b) in terms of the superficial oil velocity and percentage of water added, $U_{bs}/(U_{as} + U_{bs})$. Again all the annular viscous core flow data is practically above the $\gamma_a \simeq 1.0$ line, indicating that steady core flow is possible at very low water percentages as predicted by Moalem Maron *et al.* (1990). Moreover, for sufficiently high oil rates, $U_{as} > 200$ cm/s, which exceed the ZRC side branch [figure 14(a)], an annular viscous core pattern can be maintained almost independently of the water ratio.

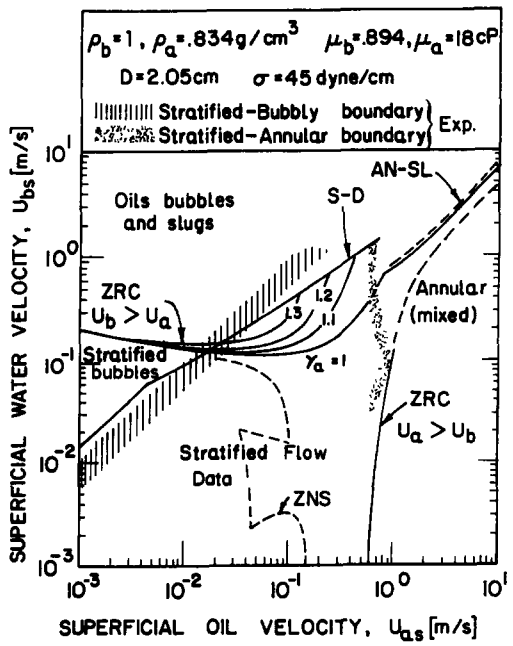

Figure 13. Flow pattern map for an oil–water system—comparison with experiments (Russell *et al.* 1959).

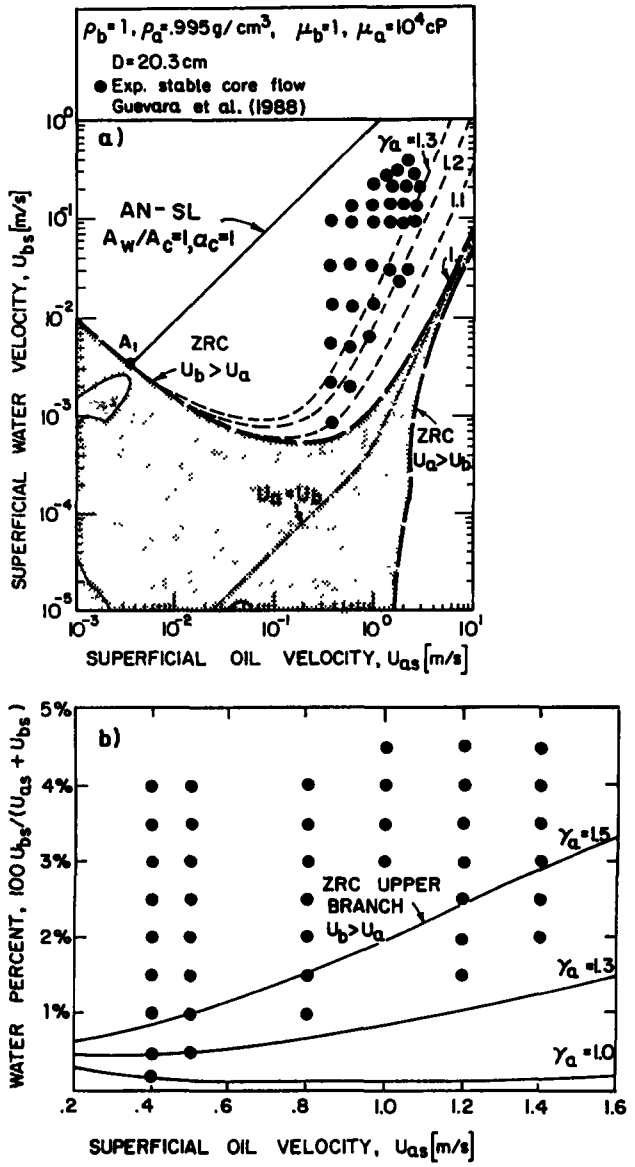

Figure 14 Flow pattern map for a highly viscous oil and water system—comparison with experiments.

On the other hand, at some lower oil rate, a minimum water addition is required as predicted by the upper ZRC branch. Core flow can be maintained up to a maximum water percentage, given by the AN–SL boundary, beyond which a transition to slug flow is predicted to take place. The intersection of the AN–SL line with the upper ZRC branch [point A_1 in figure 14(a)] defines the minimum theoretical oil rate for establishing annular core flow.

The effects of the oil viscosity on the required water percentage for maintaining a steady core flow are described in figure 15 in comparison with reported experimental data on the transition from a stratified configuration to core flow (Oliemans 1986). Again, the prediction of the proposed analytical boundary as defined by the ZRC line with $\gamma_a = 1$ to 1.1 is satisfactory. Both theory and experiment indicate that the required water addition for established core flow decreases as the oil viscosity increases.

The general outcome in view of figures 13–15 seems to be that the transitions from stratified to non-stratified patterns are reasonably predicted by the reality of characteristics criteria, Thus, the stratified configuration may extend beyond the ZNS line, which is more appropriate for the transition to a wavy stratified pattern.

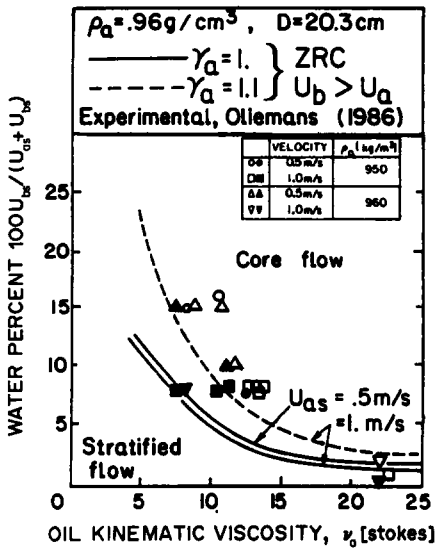

Figure 15 Effect of oil viscosity on the required water percentage addition for stabilization of a core flow configuration.

Of particular interest is the convergence of the general (liquid–liquid) formulation to the extreme of gas–liquid systems ($\rho_a/\rho_b \gg 1$, $\mu_a/\mu_b \ll 1$). Figures 16(a–c) include three sets of data for air–water systems with $D = 2.5$, 5.1 and 9.53 cm. Note first, that the upper ZRC branch (for $U_a \equiv U_G < U_b \equiv U_w$) is located beyond the range of the figure (at $U_{Gs} < 1$ cm/s).

Figures 16(a–c) indicate consistently that in horizontal gas–liquid systems and in the range of $U_{GS} \gg U_{WS}$ (and $U_G/U_W \gg 1$) the ZNS line (with a turbulent water layer) and the ZRC side branch become closer, implying that the stratified/annular transition can be predicted by either stability or reality of characteristics. On the other hand, in the range of comparable phases velocities, the ZNS and ZRC criteria move away from each other, and the data follows the ZNS boundary. This

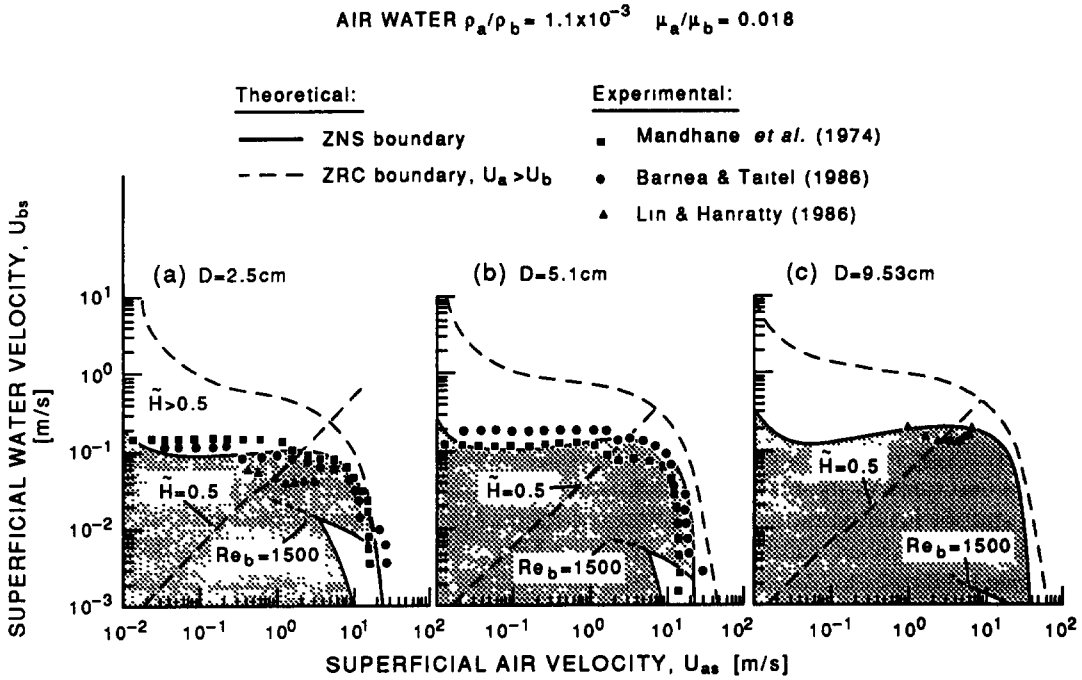

Figure 16 The ZNS and ZRC boundaries for air–water systems—comparison with experimental data on the stratified/non-stratified boundary.

is in contrast with oil–water liquid–liquid systems where the ZNS and ZRC lines converge along the upper ZRC branch, where $U_b \equiv U_w \gg U_a \equiv U_{oil}$, and diverge for $U_a \geqslant U_b$. The conditions under which the stability and well-posedness are practically identical have been widely discussed by the authors elsewhere (Brauner & Moalem Maron 1992).

Clearly, in the range where the ZNS and the ZRC boundaries are practically identical, either can be used to predict the stratified/non-stratified flow pattern transition. In the range where the ZNS and ZRC lines diverge, a "buffer" region is formed between them which is, in principle, characterized by the existence of interfacial disturbances, and as such bears a real potential for flow pattern transition. Whether these disturbances trigger the departure from a stratified configuration (due to blockage, for instance) depends on the relative thicknesses of the layers; for if $H/D \simeq 0.5$ to 1, it is likely that the evolution of the interfacial disturbances will result in tube blockage. Indeed, this is the case in gas–liquid (air–water) systems, as indicated in figures 16(a–c), where the "buffer" region is mostly above $\tilde{H} = 0.5$ and thus corresponds to relatively thick water layers. Consequently, the departure from a stratified pattern (to slug flow) in air–water systems occurs along the ZNS boundary (Brauner & Moalem Maron 1991).

On the other hand, in the liquid–liquid systems of figures 13 and 14(a,b), the lines $H/D = 0.5$ (not marked in the figures) fall above the ZRC boundary, indicating that the "buffer" regions in these cases correspond to $H/D \ll 1$, whereby a wavy stratified configuration can persist and the departure from stratified flow is delayed and predicted according to the ZRC boundaries.

4. CONCLUSIONS

The tools for constructing general two-fluid flow pattern maps in horizontal flows are proposed. The various flow patterns relevant to liquid–liquid systems have been identified and discussed for different viscosity and density ratios. It is shown that subzones of stratified–dispersed patterns may appear in the region where stable stratification is expected in view of stability considerations. By reducing the density differential, as encountered in liquid–liquid systems, the regions of dispersed patterns extend on account of the range of continuous stratified layers.

The range of stable stratification is defined here in view of the lower bound obtained from stability analysis (ZNS) and the upper bound derived from conditions for reality of characteristics (ZRC). Previous studies concerned with gas–liquid flows, relate mainly to instability criteria (or the simplified Bernoulli criterion) in predicting the stratified/non-stratified transition. Here, however, the departure from a stratified configuration to other bounding patterns is shown to be associated with a "buffer" zone formed between the ZNS and ZRC boundaries.

Finally, as the present study represents a first attempt to model liquid–liquid flow pattern transitions, while the available data is limited, wide experimental data for various two-fluid pairs is still required in order to further validate and extend the proposed models. An experimental phase is presently underway.

REFERENCES

BANERJEE, S. 1985 Multified modelling of two-phase flow: problems and potential. Presented at the *2nd Int. Conf. on Multiphase Flow*, London.

BARNEA, D. & TAITEL, Y. 1986 Flow pattern transition in two phase gas–liquid flows. In *Encyclopaedia of Fluid Mechanics* (Edited by CHEREMISINOFF, N. P.), pp. 403–474. Gulf, Houston, TX.

BRAUNER, N. 1990 On the relations between two-phase flow under reduced gravity and earth experiments. *Int. Commun. Heat Mass Transfer* **17,** 271–282.

BRAUNER, N. 1991 Two-phase liquid–liquid annular flow. *Int. J. Multiphase Flow* **17,** 59–76.

BRAUNER, N. & MOALEM MARON, D. 1989 Two-phase liquid–liquid stratified flow. *PhysicoChem. Hydrodynam.* **11,** 487–506.

BRAUNER, N. & MOALEM MARON, D. 1991 Analysis of stratified/non-stratified transitional boundaries in horizontal gas–liquid flows. *Chem. Engng Sci.* **46,** 1849–1859.

BRAUNER, N. & MOALEM MARON, D. 1992 Stability analysis of stratified liquid–liquid flow. *Int. J. Multiphase Flow* **18,** 103–121.

CHARLES, M. E., GOVIER, G. W. & HODGSON, G. W. 1961 The horizontal pipeline flow of equal density oil-water mixtures. *Can. J. Chem. Engng* **39,** 27–36.

GUEVARA, E., ZAGUSTIN, K., ZUBILLAGA, Y. & TRALLERS, J. L. 1988 Core–annular flow: the most economical method for the transportation of viscous hydrocarbons. Presented at the *4th Int. Conf. on Tar-Sands and Bitumens*, Edmonton, Alberta, paper No. 194.

HANRATTY, T. J. 1987 Gas–liquid flow in pipelines. *PhysicoChem. Hydrodynam.* **9,** 101–114.

HASSON, D., MANN, U. & NIR, A. 1970 Annular flow of two immiscible liquids: I. Mechanisms. *Can. J. Chem. Engng* **48,** 514–520.

HINZE, J. O. 1955 Fundamentals of the hydrodynamic mechanism of splitting in dispersion processes. *AIChE Jl* **1,** 289–295.

LIN, P. Y. & HANRATTY, T. J. 1986 Prediction of the initiation of slugs with linear stability theory. *Int. J. Multiphase Flow* **12,** 79–98.

MANDHANE, J. M., GREGORY, G. A. & AZIZ, K. 1974 A flow pattern map for gas liquid flow in horizontal pipes. *Int. J. Multiphase Flow* **1,** 537–553.

MOALEM MARON, D., BRAUNER, N. & KRUKA, V. R. 1990 The mechanisms of two phase liquid–liquid viscous core flow. In *Proc. 6th Miami Int. Symp. Heat and Mass Transfer.* In press.

OLIEMANS, R. V. A. 1986 The lubricating-film model for core–annular flow. Ph.D. Dissertation, Delft Univ.

RUSSELL, T. W. F. & CHARLES, M. E. 1959 The effect of the less viscous liquid in the laminar flow of two immiscible liquids. *Can. J. Chem. Engng* **37,** 18–24.

RUSSELL, T. W. F., HODGSON, G. W. & GOVIER, G. W. 1959 Horizontal pipeline flow of oil and water. *Can. J. Chem. Engng* **37,** 9–17.

WU, H. L., DUIJVESTIJN, P. E. M., PATERNO, J. & GUEVARA, E. 1986 Core–annular flow: a solution to pipeline transportation of heavy crude oils. *Rev. Tech. Intevep.* **6**(1), 17–22.